

# The Milky Way’s bulge star formation history as constrained from its bimodal chemical abundance distribution

Jianhui Lian<sup>1\*</sup>, Gail Zasowski<sup>1</sup>, Sten Hasselquist<sup>1</sup>, David M. Nataf<sup>2</sup>, Daniel Thomas<sup>3</sup>, Christian Moni Bidin<sup>4</sup>, José G. Fernández-Trincado<sup>5</sup>, D. A. Garcia-Hernandez<sup>6,7</sup>, Richard R. Lane<sup>8</sup>, Steven R. Majewski<sup>9</sup>, Alexandre Roman-Lopes<sup>10</sup>, Mathias Schultheis<sup>11</sup>

<sup>1</sup>Department of Physics & Astronomy, University of Utah, Salt Lake City, UT 84112, USA

<sup>2</sup>Center for Astrophysical Sciences and Department of Physics and Astronomy, The Johns Hopkins University, Baltimore, MD 21218

<sup>3</sup>Institute of Cosmology and Gravitation, University of Portsmouth, Burnaby Road, Portsmouth, UK, PO1 3FX

<sup>4</sup>Universidad Católica del Norte, Instituto de Astronomía, Av. Angamos 0610, Antofagasta, Chile

<sup>5</sup>Instituto de Astronomía y Ciencias Planetarias, Universidad de Atacama, Copayapu 485, Copiapó, Chile

<sup>6</sup>Instituto de Astrofísica de Canarias, 38205 La Laguna, Tenerife, Spain

<sup>7</sup>Universidad de La Laguna (ULL), Departamento de Astrofísica, E-38206 La Laguna, Tenerife, Spain

<sup>8</sup>Instituto de Astrofísica, Pontificia Universidad Católica de Chile, Av. Vicuña Mackenna 4860, 782-0436 Macul, Santiago, Chile

<sup>9</sup>Department of Astronomy, University of Virginia, Charlottesville, VA 22904-4325, USA

<sup>10</sup>Departamento de Física, Facultad de Ciencias, Universidad de La Serena, Cisternas 1200, La Serena, Chile

<sup>11</sup>Observatoire de la Côte d’Azur, Laboratoire Lagrange, 06304 Nice Cedex 4, France

27 July 2020

## ABSTRACT

We conduct a quantitative analysis of the star formation history (SFH) of the Milky Way’s bulge by exploiting the constraining power of its stellar  $[\text{Fe}/\text{H}]$  and  $[\text{Mg}/\text{Fe}]$  distribution functions. Using APOGEE data, we confirm the previously-established bimodal  $[\text{Mg}/\text{Fe}]$ – $[\text{Fe}/\text{H}]$  distribution within 3 kpc of the inner Galaxy. Compared to that in the solar vicinity, the high- $\alpha$  population in the bulge peaks at a lower  $[\text{Fe}/\text{H}]$ . To fit these observations, we use a simple but flexible star formation framework, which assumes two distinct stages of gas accretion and star formation, and systematically evaluate a wide multi-dimensional parameter space. We find that the data favor a three-phase SFH that consists of an initial starburst, followed by a rapid star formation quenching episode and a lengthy, quiescent secular evolution phase. The metal-poor, high- $\alpha$  bulge stars ( $[\text{Fe}/\text{H}] < 0.0$  and  $[\text{Mg}/\text{Fe}] > 0.15$ ) are formed rapidly ( $< 2$  Gyr) during the early starburst. The density gap between the high- and low- $\alpha$  sequences is due to the quenching process. The metal-rich, low- $\alpha$  population ( $[\text{Fe}/\text{H}] > 0.0$  and  $[\text{Mg}/\text{Fe}] < 0.15$ ) then accumulates gradually through inefficient star formation during the secular phase. This is qualitatively consistent with the early SFH of the inner disk. Given this scenario, a notable fraction of young stars (age  $< 5$  Gyr) is expected to persist in the bulge. Combined with extragalactic observations, these results suggest that a rapid star formation quenching process is responsible for bimodal distributions in both the MWs stellar populations and in the general galaxy population and thus plays a critical role in galaxy evolution.

**Key words:** The Galaxy: abundances – The Galaxy: bulge – The Galaxy: formation – The Galaxy: evolution – The Galaxy: stellar content – The Galaxy: structure.

## 1 INTRODUCTION

The chemical compositions of stars are valuable fossil records that preserve — in many cases — the chemistry

\* jianhui.lian@astro.utah.edu

of the interstellar medium (ISM) from which the stars were born. Observations of large samples of stars formed at different epochs therefore allow one to unfold the chemical enrichment and star formation history (SFH) of the host system with unprecedented accuracy. The Milky Way (MW) is an ideal laboratory to conduct such analysis on a galaxy scale where chemistry observations of large numbers of individual stars are achievable. These observations have relatively recently extended to the Galactic bulge (compared to, e.g., the solar neighborhood and halo), which is the only example of a massive galaxy center that can be studied in this way. Our bulge is therefore of great importance to understand the stellar population and formation history of galactic bulges in general.

Early studies of MW bulge chemistry revealed the existence of multiple stellar populations with a wide range of metallicity, spanning  $\sim -1$  to  $\sim +0.5$  dex (Whitford & Rich 1983; Rich 1988; McWilliam & Rich 1994). Large effort has since been devoted to mapping the detailed metallicity distribution function (MDF) in the Galactic bulge using tracers such as Red Giant Branch stars (Zoccali et al. 2008; Rich et al. 2012; Uttenthaler et al. 2012; Johnson et al. 2013; Schultheis et al. 2017; Rojas-Arriagada et al. 2017; García Pérez et al. 2018a), red clump stars (Hill et al. 2011; Ness et al. 2013; Zoccali et al. 2017; Rojas-Arriagada et al. 2014), and even subgiant and dwarf stars (Bensby et al. 2013). The MDF in the bulge as derived in different works shows noticeable difference in peak structure, described as either two strong  $[\text{Fe}/\text{H}]$  peaks (with a supersolar component at  $> +0.3$  and a subsolar one at  $< -0.4$ ; e.g., Hill et al. 2011; Schultheis et al. 2017) or multiple, less strong peaks within the same metallicity range (e.g., Bensby et al. 2013; Ness et al. 2013).

In addition to the MDF,  $\alpha$ -element abundances serve as important constraints on the SFH of stellar populations, in both our Galaxy and the general galaxy population. In particular, the relative abundance ratio of  $\alpha$ -elements to iron ( $[\alpha/\text{Fe}]$ ) is a powerful diagnostic of star formation timescale, as rapid star formation can be recognized from an enhanced  $[\alpha/\text{Fe}]$  in stellar composition (Matteucci 1994; Thomas et al. 2010). It has become increasingly clear that the bulge is composed of at least two distinct populations: a dominant one comprising old, metal-poor, and  $\alpha$ -enhanced stars, and a less numerous one comprising intermediate-age, metal-rich stars with solar-like  $[\alpha/\text{Fe}]$  (e.g., Babusiaux et al. 2010; Hill et al. 2011; Schultheis et al. 2017; Rojas-Arriagada et al. 2019; Queiroz et al. 2020).

A long-running debate persists over whether the  $\alpha$ -element enhancement in the old bulge stellar populations is identical with that of thick disk stars, such as those in the solar vicinity. The important physical question underlying this discussion is whether the bulge and thick disk share the same early SFH or not. Slightly different, perhaps systematically higher,  $[\alpha/\text{Fe}]$  abundances in the old bulge stars were suggested in some works (Cunha & Smith 2006; Zoccali et al. 2006; Lecureur et al. 2007; Fulbright et al. 2007; Zsawski et al. 2019). On the other hand, other studies found no significant difference (Meléndez et al. 2008; Alves-Brito et al. 2010), evidence that favors a picture with no distinct chemical “bulge” structure besides the inner thick disk in the Galactic center (Fragkoudi et al. 2018; Di Matteo et al.

2019). In this sense, the Milky Way would be a pure disk galaxy with a buckled bar (e.g., Nataf 2017).

On the theoretical side, impressive progress has been made to interpret these observed chemical distributions in the bulge. Matteucci & Brocato (1990) performed one of the pioneering chemical evolution modelling of the Galactic bulge, which traces not only the enrichment history of global metal content but also Fe, Si, Mg, and O individually. By comparing the prediction of various models with the observed MDF from Rich (1988), the authors reached the conclusion that the bulge formed on a much shorter timescale ( $< 0.5$  Gyr) than the disk, with more efficient star formation and a flatter IMF. Following the observations of two distinct stellar populations in the bulge, many chemical evolution models have been developed to account for possible multiple formation channels or phases in the bulge (e.g., Bekki & Tsujimoto 2011; Grieco et al. 2012; Tsujimoto & Bekki 2012; Haywood et al. 2018; Matteucci et al. 2019). Haywood et al. (2018) proposed a heuristic two-phase SFH connected by a rapid quenching episode to explain the density dip in the MDF and  $[\alpha/\text{Fe}]$  distribution functions ( $\alpha$ -DF) observed in the APOGEE survey (Majewski et al. 2017). By exploring a broad radial range of the inner Galaxy ( $R_{GC} < 7$  kpc), Haywood et al. (2018) suggested that the bulge and inner disk are indistinguishable in terms of chemical properties and that their chemical evolution has followed a similar path.

Although enormous progress has been made in modelling the chemical evolution in the bulge, most works have been conducted in a qualitative way, in which viable models are commonly assessed based on visual inspection on the comparison with observations. In this work we aim to perform a quantitative analysis using recent chemical data from the APOGEE survey in order to reveal the detailed star formation and enrichment history of the Galactic bulge. The paper is organized as follows: We introduce the sample selection and the observed MDF and  $\alpha$ -DF in §2. In §3 we describe the chemical evolution model used in this work and explain the systematic search for the best-fit model and the result of this search. More discussions about interpretation of the best-fit model and room for improvement of the model are presented in §4. We briefly summarize our results in §5.

## 2 DATA

### 2.1 Sample selection

Our sample is selected from the Apache Point Observatory Galactic Evolution Experiment survey (APOGEE; Majewski et al. 2017), an on-going core project of the Sloan Digital Sky Survey IV (SDSS-IV; Blanton et al. 2017). APOGEE provides high-resolution, near-infrared spectra for  $\sim 5 \times 10^5$  stars throughout the Milky Way bulge, disc, and halo (Zsawski et al. 2013, 2017), using custom spectrographs (Wilson et al. 2019) at 2.5 m Sloan Telescope at the Apache Point Observatory (Gunn et al. 2006), and the 2.5 m Irénée du Pont telescope (Bowen & Vaughan 1973) at Las Campanas Observatory. Radial velocities, stellar parameters, and chemical abundances are determined from the spectra, using custom pipelines described in Nidever et al. (2015), García Pérez et al. (2016) and Jönsson et al. (2020). In

this work we use the parameters and abundances of a recent APOGEE internal release that includes reduced observations until November 2019 (using the DR16 pipeline; Ahumada et al. 2020), and spectro-photometric distances based on the procedure described in Rojas-Arriagada et al. (2017).

To remove stars with problematic spectra or unreliable parameter determinations, we adopt a signal-to-noise (SNR) cut of 60 and use the APOGEE spectroscopic flags<sup>1</sup> to select stars with `EXTRATARG== 0`; the 1st, 4th, 9th, 16th and 17th bit of `STARFLAG== 0`, which correspond respectively to `COMMISSIONING`, `LOW_SNR`, `PERSIST_HIGH`, `SUSPECT_RV_COMBINATION`, and `SUSPECT_BROAD_LINES`; and the 19th and 23th bit of `ASCAPFLAG== 0`, which correspond to `METALS_BAD` and `STAR_BAD`. Since elemental abundance determinations in APOGEE tend to be less reliable at low effective temperature,  $T_{\text{eff}}$ , we further exclude stars with  $T_{\text{eff}} < 3200$  K. We have tested that our results do not change significantly when adopting an effective temperature cut at 3500 K for the sample selection.

In this work, we analyze the  $[\text{Mg}/\text{Fe}]$ - $[\text{Fe}/\text{H}]$  abundance plane. We adopt magnesium ( $[\text{Mg}/\text{Fe}]$ ) to trace the  $\alpha$  abundance, as it is shown to be the  $\alpha$  element most reliably measured by the pipeline, with least dependence on effective temperature, (Jönsson et al. 2018; Rojas-Arriagada et al. 2019, Jönsson et al. in prep). Note that the  $[\text{Fe}/\text{H}]$  and other elements to iron ratio,  $[\text{X}/\text{Fe}]$ , of APOGEE stars are not populated when a `PARAM_MISMATCH_WARN` flag is set. This flag is activated when the difference between the  $[\text{Fe}/\text{H}]$  abundance determined from Fe spectral features and the  $[\text{M}/\text{H}]$  (the abundance of total metal content determined from the entire spectrum) exceeds 0.1 dex. The reason for this discrepancy is not yet completely clear to the APOGEE team, but the stars for which this flag is set are generally metal rich ( $[\text{Fe}/\text{H}] > 0.0$ ) and cool ( $T_{\text{eff}} < 4000$  K). We obtain 15% more stars when using  $[\text{M}/\text{H}]$  instead of  $[\text{Fe}/\text{H}]$  for the sample selection. Because stars with this mismatch are mostly metal rich, the sample selected in this work based on  $[\text{Fe}/\text{H}]$  is likely biased with underestimated surface density at the high metallicity end. We will discuss the potential effect on our results in §3.4.

We select stars in the Galactic bulge region on our side with Galactocentric distances within 3 kpc ( $R_{\text{GC}} < 3$  kpc). Since the APOGEE sampling is irregular at different heights above the mid-plane, we focus on the mid-plane ( $|Z| < 0.5$  kpc), where the observations tend to be distributed more homogeneously. Our stellar sample on the mid-plane contains 4454 stars. To obtain the integrated abundance distribution for the whole bulge region, we adopt the metallicity- and  $\alpha$ -dependent scale height derived by Bovy et al. (2012, see more details in §2.3).

Figure 1 shows the spatial distribution of APOGEE stars (grey dots) and our sample (orange dots) in the  $R_{\text{GC}} - Z$  plane (left-hand panel) and the  $X - Y$  plane (right-hand panel). The positions of the Sun and the Galactic center are marked for reference.

## 2.2 Sample abundance distribution in the plane

The left panel of Figure 2 shows the observed density distribution of  $[\text{Mg}/\text{Fe}]$ - $[\text{Fe}/\text{H}]$  for the sample on the mid-plane of the bulge region. A bimodal distribution is present, with a density gap at solar metallicity and  $[\text{Mg}/\text{Fe}] \sim 0.15$ , suggesting at least two phases of star formation in the Galactic bulge. This gap in the  $[\text{Mg}/\text{Fe}]$ - $[\text{Fe}/\text{H}]$  plane was also reported in Rojas-Arriagada et al. (2019) based on APOGEE DR14 data. The metal-rich and metal-poor populations follow two  $[\text{Mg}/\text{Fe}]$ - $[\text{Fe}/\text{H}]$  sequences with a small vertical offset in  $[\text{Mg}/\text{Fe}]$ , consistent with the finding in Hill et al. (2011). The top and right sub-panels of Figure 2 show the projected distribution functions in  $[\text{Fe}/\text{H}]$  and  $[\text{Mg}/\text{Fe}]$  (the MDF and  $\alpha$ -DF), respectively, in black solid lines. The grey dashed lines indicate the MDF and  $\alpha$ -DF of the inner disk ( $4 < R_{\text{GC}} < 8$  kpc) taken from Lian et al. (2020a). The bulge MDF shows a strong, wide peak at  $[\text{Fe}/\text{H}] \sim 0.37$  dex, while the  $\alpha$ -DF exhibits a clear bimodal distribution, with two peaks at  $[\text{Mg}/\text{Fe}] \sim 0.32$  and  $\sim 0.05$  dex, respectively and an interesting bump at  $[\text{Mg}/\text{Fe}] \sim 0.2$ .

A similar bimodal distribution has been found across a large portion of the disk from the inner Galaxy to the solar vicinity (Nidever et al. 2014; Hayden et al. 2015). The metal-poor, high- $\alpha$  branch is nearly invariant in chemical abundance space throughout the Galaxy except that the density distribution is more extended in both  $[\text{Fe}/\text{H}]$  and  $[\text{Mg}/\text{Fe}]$  and peaks at a slightly lower  $[\text{Fe}/\text{H}]$  in the bulge than in the solar vicinity. In contrast, the metal-rich, low- $\alpha$  branch shifts systematically toward lower metallicity with increasing Galactic radius. This radial variation pattern suggests that the Galactic bulge and disk share a common early star formation history but follow different evolution paths in the more recent past, when the chemical thin disk (i.e., the low- $\alpha$  branch) formed.

## 2.3 Integrated abundance distribution

It has been shown that the vertical structure of stellar populations is dependent on their metallicity and  $[\alpha/\text{Fe}]$  (e.g., Bovy et al. 2012, 2016). More metal-poor and  $\alpha$ -enhanced stellar populations tend to have larger scale height and therefore dominate the stellar density distribution at larger vertical distance from the mid-plane. In the APOGEE survey, pointings targeting the inner Galaxy do not provide complete vertical or even angular coverage, but are localized to certain sky regions by design. The effect is that the observational sampling of the APOGEE survey at different heights in the bulge region is complex and irregular. To derive abundance distributions of the global bulge region, simply summing up APOGEE observations at different heights, given the significant vertical abundance gradient (García Pérez et al. 2018b), will introduce considerable bias for which it is difficult to account.

An effective alternative approach is to use the observed distribution in the mid-plane and account for the vertical distribution based on the known vertical structure of mono-abundance sub-populations. So far such mono-abundance analysis has only been conducted for the disk outside the bulge region (Bovy et al. 2012; Mackereth et al. 2017). We therefore extrapolate the abundance-dependent disk scale height from Bovy et al. (2012), taking the effect of the

<sup>1</sup> <http://www.sdss.org/dr16/algorithms/bitmasks/>

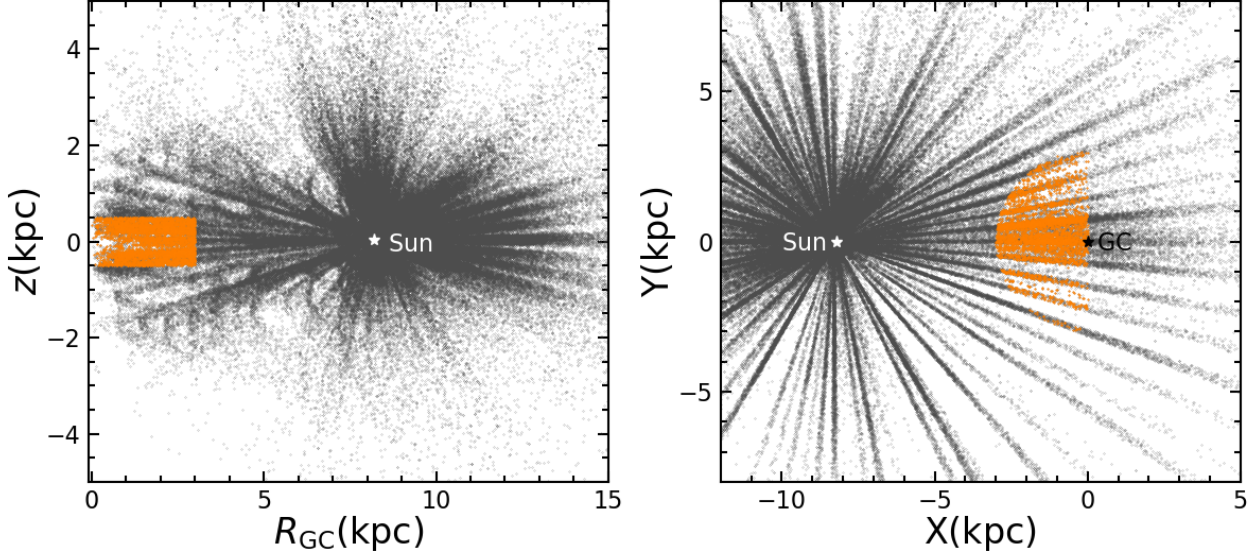


**Figure 1.** Spatial distribution of stars in the  $R_{GC} - Z$  plane (left-hand panel) and  $X - Y$  plane (right-hand panel). APOGEE stars meeting the flag and SNR requirements as described in the text (§2.1) are indicated by gray dots; stars in our final bulge sample with further spatial and effective temperature limits are denoted as orange dots.

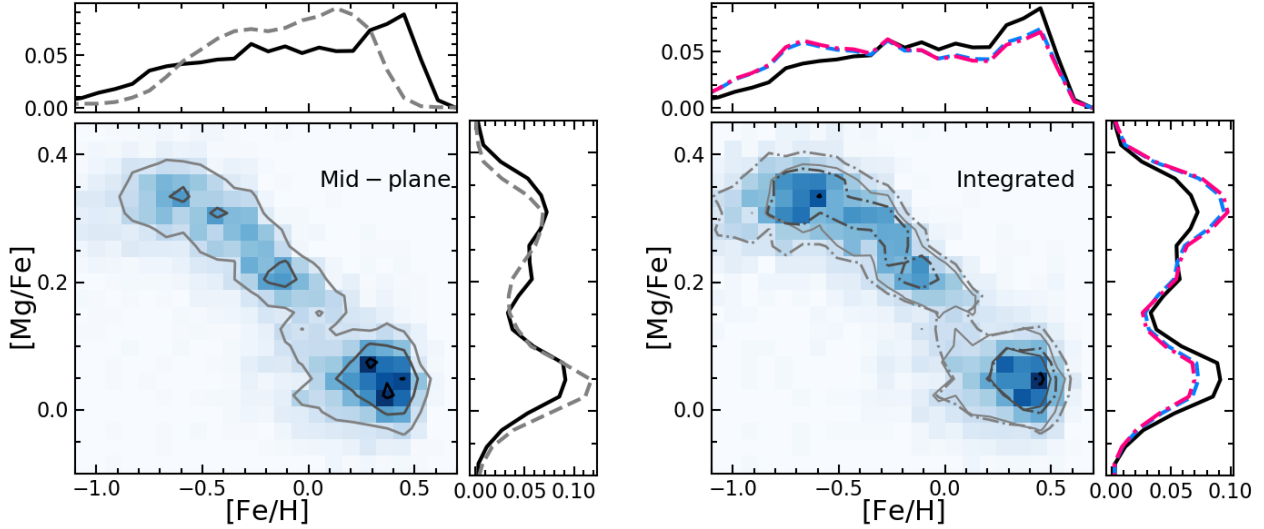


**Figure 2.** Density distribution of  $[Mg/Fe]-[Fe/H]$  for stars on the mid-plane (left-hand panel) and for the whole bulge region (right-hand panel). The projected distribution functions in  $[Fe/H]$  and  $[Mg/Fe]$  are normalized to the total number of stars and shown at the top and right sub-panels, respectively. Grey dashed lines in the left-hand sub-panels indicate the MDF and  $\alpha$ -DF in the inner disk taken from Lian et al. (2020a). In the right-hand panel, the dash-dotted and solid contours outline the integrated density distribution with and without consideration of disk flare, respectively. The red dash-dotted and blue dashed curves in sub-panels denote the corresponding MDF and  $\alpha$ -DF, respectively. Black solid curves are the original MDF and  $\alpha$ -DF on the mid-plane for reference.

flare into account, to obtain the vertical structure of mono-abundance sub-populations in the bulge region. When no disk flare is considered, the scale heights of the high- and low- $\alpha$  populations ( $[Mg/Fe] > 0.15$  and  $[Mg/Fe] < 0.15$ ) are 562 and 233 pc on average, respectively. For the flare, we adopt an average value of  $R_{flare}^{-1} = -0.1 \text{ kpc}^{-1}$  for the low- $\alpha$  population (see Fig. 12 in Bovy et al. 2016) and assume no flare for the high- $\alpha$  population as in that same paper. This choice of flare strength for the low- $\alpha$  population implies a

1.52 times lower scale height at  $R_{GC} = 3 \text{ kpc}$  compared to at the solar radius.

For each  $[Fe/H]-[\alpha/Fe]$  bin, assuming an exponential disk in the vertical direction, the integrated surface density is derived following

$$d_{tot} = \frac{d_{0.5}}{1 - e^{-\frac{0.5}{h_z}}}, \quad (1)$$

where  $d_{0.5}$  is the observed surface density within  $|Z| <$

0.5 kpc and  $h_z$  is the scale height of the given mono-abundance sub-population.

It is worth pointing out that this approach implicitly assumes a homogeneous vertical structure within the bulge region. It is known that the MW's bulge contains a buckled bar which complicates the situation. The Galactic bar barely affects the vertical distribution of metal-poor, high- $\alpha$  stars as evidenced by the consistent scale height ( $\sim 500$  pc, Portail et al. 2017) with their counterparts in the disk (Bovy et al. 2012). Therefore we assume that the structure of these stars near the solar neighborhood is applicable to the bulge. In contrast, the metal-rich, low- $\alpha$  stars in the bar are generally thicker than their counterparts in the disk due to bar buckling (Wegg & Gerhard 2013). Thus extrapolation of the structure of these stars from the disk could possibly underestimate their scale height in the bulge and therefore underestimate their integrated surface density.

Note that the original abundance distribution on the mid-plane is equivalent to the integrated abundance distribution when assuming the same scale heights for all stars. Although the scale height of metal-rich, low- $\alpha$  stars in the bar is higher than that in the disk, it is still lower than the scale height of the metal-poor, high- $\alpha$  stars (Portail et al. 2017). Hence taking the original observations on the mid-plane to represent the whole bulge would overestimate the scale height and thus the relative surface density of metal-rich, low- $\alpha$  stars. Therefore the original and integrated MDF and  $\alpha$ -DF could be considered as two extreme cases with overestimated and underestimated metal-rich, low- $\alpha$  stars, respectively. Since we lack information on the scale height of the mono-abundance population in the bulge, we use both the original and the integrated observations to constrain the bulge SFH as described in the next section.

The right panel of Figure 2 shows the integrated density distribution of  $[\text{Mg}/\text{Fe}]$ - $[\text{Fe}/\text{H}]$  and the projected MDF and  $\alpha$ -DF for the whole bulge region. The density map and solid contours show the integrated density distribution without consideration of the disk flare, while the dash-dotted contours outline the distribution with the disk flare taken into account. Comparing to the density distribution on the mid-plane (left panels), the integrated one exhibits a more prominent metal-poor, high- $\alpha$  branch. This is because the denominator in Eq. 1 is larger for the metal-poor population, given their larger scale height compared to the metal-rich population.

In Figure 2, the integrated MDFs and  $\alpha$ -DFs with and without consideration of the disk flare are indicated as red dash-dotted and blue dashed curves, respectively. They are significantly different from their equivalent distributions in the mid-plane (black solid) with relatively more metal-poor, high- $\alpha$  stars due to those populations larger scale height. However, the integrated MDF and  $\alpha$ -DF barely change when taking the disk flare into account. There is an interesting bump in the  $\alpha$ -DF at  $[\text{Mg}/\text{Fe}] \sim +0.2$ , which extends the metal-poor, high- $\alpha$  branch in the MDF. The existence of this population reduces the significance of the bimodality in both the MDF and  $\alpha$ -DF.

### 3 CHEMICAL EVOLUTION MODEL

#### 3.1 Key ingredients

To interpret observed chemical abundances in gaseous and stellar components of local galaxies, we developed a numerical chemical evolution model that accounts for three basic astrophysical processes involved in chemical enrichment: star formation, gas accretion, and galactic winds (Lian et al. 2018a,b,c, 2019). The model was further enhanced to be able to predict multiple elemental abundances of individual stars, in order to compare chemical evolution tracks with the enormous sets of stellar observations in the Milky Way (Lian et al. 2020b, submitted). Here, we briefly introduce basic assumptions and inputs of the model and recommend Lian et al. (2018a) and Lian et al. (2020b) to the reader for a more detailed description of the model development.

We adopt the Kennicutt-Schmidt (KS) star formation law (Kennicutt 1998) that connects the gas mass with star formation rate (SFR), but we allow the coefficient that regulates star formation efficiency (SFE:  $\text{SFR}/M_{\text{gas}}$ ) to vary (Table 1). This free coefficient is normalized to the original coefficient of the KS law (i.e.,  $2.5 \times 10^{-4}$ ). A Kroupa (2001) stellar initial mass function is adopted in the model. Considering the relatively high mass of our Galaxy, and the fact that metal outflow strength scales inversely with galaxy mass (Chisholm et al. 2018; Lian et al. 2018a), we assume no outflow in the model for the inner Milky Way.

Metal production from asymptotic giant branch (AGB) stars, Type-Ia supernovae (SN-Ia), and core-collapse supernovae (CCSNe) are included in the model. Instead of assuming instantaneous mixing, we take the lifespan of stars fully into account, with metal-enriched material from evolved stars released to mix with ISM at the end of their evolution. We use metallicity-dependent AGB yields from Ventura et al. (2013) and SN-Ia yields from Iwamoto et al. (1999). To study the effect of uncertainty in yields on our results, we use two sets of metallicity-dependent CCSNe yields from Chieffi & Limongi (2004, hereafter CL04) and Kobayashi et al. (2006, hereafter K06) and explore the best-fit model for each of them. To account for the time delay of SN-Ia since the birth of the SN-Ia-producing binary system, we adopt an empirical power-law SN-Ia delay-time distribution (DTD) with slope  $-1.1$ , which is calibrated to observed SN-Ia rates (Maoz et al. 2012). We left the parameter  $f_{\text{SN-Ia}}$  free (Table 1), which regulates the global SN-Ia rate – i.e., the fraction of stars within  $3 < M_* < 16 M_{\odot}$  that are SN-Ia progenitors – to test whether it could be constrained by the abundance observations. We adopt a minimum SN-Ia delay time of 35 Myr, which is widely used in chemical evolution models in the literature (e.g., Matteucci et al. 2009). However, we will discuss the effect of adopting a different minimum SN-Ia delay time in §4.3.

#### 3.2 Underestimate of magnesium production

When comparing observed  $\alpha$  element-iron abundance ratios,  $[\alpha/\text{Fe}]$ , with our chemical evolution models, we noticed evidence that the magnesium production in the K06 and CL04 CCSNe yields may be underestimated. To illustrate this, Figure 3 shows the comparison between models with these yields and observed abundances in the  $[\text{O}/\text{Fe}]$ - $[\text{Fe}/\text{H}]$  and  $[\text{Mg}/\text{Fe}]$ - $[\text{Fe}/\text{H}]$  planes. Observations within  $6 <$

$R_{GC} < 7$  kpc (also with APOGEE) are used in this comparison for two reasons. On one hand, the observed sample at smaller  $R_{GC}$  in the inner Galaxy is dominated by luminous stars for which APOGEE’s oxygen abundances are in some cases less reliable (Jönsson et al. 2018; Zasowski et al. 2019). On the other hand, stellar populations in the outer Galaxy are intrinsically different from the bulge region, with far fewer high- $\alpha$  stars. As a compromise, stars within  $6 < R_{GC} < 7$  kpc are used for the comparison.

We calculate a test model for both the K06 (magenta lines) and CL04 (orange lines) yields, with adopted parameter values listed in Table 2 as the “Test model”. In Figure 3, it can be seen that at a given  $[\text{Fe}/\text{H}]$ , the offsets between the models and data are clearly larger in  $[\text{Mg}/\text{Fe}]$  (right panel) than in  $[\text{O}/\text{Fe}]$  (left panel). For the model with K06 yields, when the model track in  $[\text{O}/\text{Fe}]-[\text{Fe}/\text{H}]$  is above the high- $\alpha$  branch, the track of the same model in  $[\text{Mg}/\text{Fe}]-[\text{Fe}/\text{H}]$  lies at lower  $[\text{Mg}/\text{Fe}]$ . We have confirmed that the offset in  $[\text{Mg}/\text{Fe}]$  with respect to  $[\text{O}/\text{Fe}]$  is not dependent on the choice of model parameters.

This systematic shift between different  $\alpha$  elements is not likely to be due to systematics in the observed abundances. Based on the comparison with optical studies, oxygen and especially magnesium are both precisely and accurately measured in APOGEE (see the discussion in Jönsson et al. 2020). According to Jönsson et al. (2020), a small number of stars show signs of systematics in the abundance measurements; however, because these stars are concentrated within a limited range of chemical abundance, this behavior is unlikely to explain the discrepancy seen across a wide range of metallicity in Fig. 3.

The most likely explanation for this discrepancy is that the magnesium production with respect to oxygen in both the K06 and CL04 CCSNe yields are underestimated. The underestimation of Mg in CCSNe yields has been highlighted in Thomas et al. (1998). A similar underestimated Mg/O ratio is also reported in other chemical evolution models in the literature (Sukhbold et al. 2016; Rybizki et al. 2017; Limongi & Chieffi 2018).

As a result, the chemical evolution model struggles to match the observed  $[\text{Mg}/\text{Fe}]-[\text{Fe}/\text{H}]$  distribution with the default CCSNe magnesium yields given the adopted minimum SN-Ia delay time of 35 Myr. If no correction is applied to the Mg yields, then in order to reproduce the enhanced  $[\text{Mg}/\text{Fe}]$  of the high- $\alpha$  population, one needs to adopt a much higher minimum SN-Ia delay time. As we will discuss later on in §4.3, with this modification and the original yields, the models cannot attain as good a match to the data.

In this work, we take the oxygen production as a benchmark to estimate the relative deficiency in Mg production. We calculate the net offset between the model tracks and the data in  $[\text{Mg}/\text{Fe}]$ , with respect to  $[\text{O}/\text{Fe}]$ , at a given  $[\text{Fe}/\text{H}]$ . The average offsets in K06 and CL04 yields are  $-0.13$  and  $-0.15$  dex, respectively. We enhance the Mg production by the same offsets in these two CCSNe yields. The dashed lines in the right panel of Fig. 3 show the model tracks with enhanced Mg production. With this modification, the models are able to match the observed oxygen and magnesium abundances simultaneously with physically plausible parameters. While we adopt a constant enhancement, the modification of magnesium production required to match the data is possibly metallicity dependent (Matteucci et al. 2020). It is worth

pointing out that the difference in magnesium production between the CL04 and K06 yields is much higher than the modification adopted in this work. Therefore we expect the effect of using different yields on our results would be much higher than the modification of magnesium production.

### 3.3 Star formation framework

To conduct a systematic search for the best-fit model, we adopt a simple and flexible star formation framework modified from the one in Lian et al. (2020a), in which we propose a novel multi-phase star formation framework to explain the joint distribution function of  $[\text{Fe}/\text{H}]$  and  $[\text{Mg}/\text{Fe}]$  in the inner disk ( $4 < R_{GC} < 8$  kpc). This framework consists of an early and a recent starburst that are associated with two relatively brief gas accretion events. The early starburst is responsible for the formation of the chemical thick disk on a short timescale, while during the recent starburst, a metal-poor, moderately  $\alpha$ -enhanced population formed in the thin disk. Our model based on this multi-phase star formation history successfully reproduces the observed abundance distribution functions in the disk, especially the bimodal distribution in the  $[\alpha/\text{Fe}]-[\text{Fe}/\text{H}]$  plane. In this scenario, the well-known  $\alpha$ -bimodality arises due to a dramatically rapid decrease of star formation (i.e., star formation quenching) following the early starburst.

We adopt a similar multi-phase star formation framework to interpret the abundance distribution functions observed in the Galactic bulge. Note that the metal-poor, moderately  $\alpha$ -enhanced population observed in the disk is absent in the bulge, suggesting that the inner Galaxy is not affected by the recent gas accretion event manifested in the disk. We therefore adopt a simpler version of the star formation framework presented in Lian et al. (2020a), without the second gas infall and starburst event. There are four free parameters that characterize this star formation framework:

- Initial coefficient of the KS law during the early starburst,  $Coe_{\text{burst}}$ ;
- Time when gas accretion is switched off,  $t_{\text{acc,tran}}$ ;
- Time when coefficient of the KS law changes,  $t_{\text{SFE,tran}}$ ;
- The coefficient of the KS law after the early starburst,  $Coe_{\text{post-burst}}$ .

The initial gas accretion rate is fixed to be  $1.5 M_{\odot} \text{yr}^{-1} \text{kpc}^{-2}$ , and no gas accretion is assumed to occur after  $t_{\text{acc,tran}}$ . Thus in total, there are five free parameters in our model: four parameters describing the SFH plus  $f_{\text{SN-Ia}}$ , the parameter regulating the global SN-Ia rate (§3.1).

### 3.4 Best-fit model

#### 3.4.1 Systematic search for the best-fit model

Although abundance distribution functions have frequently been used to infer the bulge SFH (e.g., Haywood et al. 2018; Matteucci et al. 2019), the result is usually evaluated via a qualitative comparison to the data without a systematic, quantitative search across a range of possible solutions. One goal of this work is to determine the SFH of the Galactic bulge region in a quantitative way by exploring an extensive parameter space and assessing the robustness of the result.

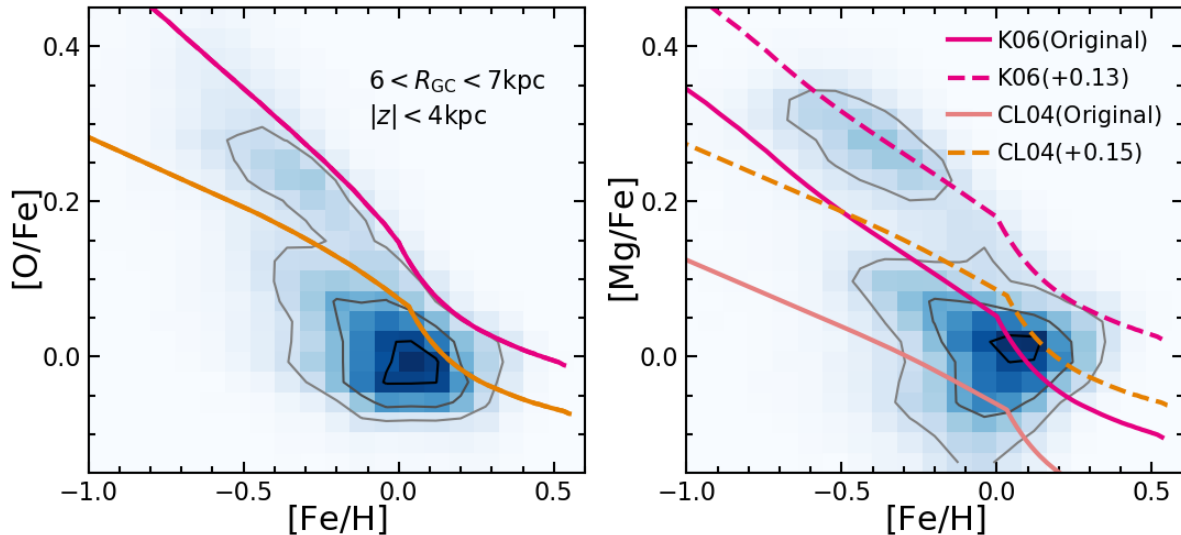


**Figure 3.** Prediction of models with original or Mg-enhanced CCSNe yields in  $[O/Fe]$ - $[Fe/H]$  (left-hand panel) and  $[Mg/Fe]$ - $[Fe/H]$  (right-hand panel). Solid lines indicate models with original CCSNe yields while dashed lines are models with Mg-enhanced yields. Observed stellar abundances in the disk within  $6 < R_{GC} < 7$  kpc and  $|Z| < 4$  kpc are shown in the blue density map and black contours.

To this end, we create a 5-D parameter grid and run our chemical evolution model for each combination of the parameters. The range and step size of each parameter grid dimension are listed in Table 1. These values are chosen based on our experience to achieve a compromise between a wide coverage of parameter space and acceptable computation time. In total, 216,000 models are calculated for each of the CL04 and K06 CCSNe yields. Then, given the derived SFH and chemical evolution history for each model, we generate a mock stellar catalog of surviving stars, considering observational abundance uncertainties. A conservative uncertainty of 0.02 dex and 0.03 dex is adopted for  $[Fe/H]$  and  $[Mg/Fe]$ , respectively, which is generally higher than the uncertainties in the data release catalog by a factor of  $\sim 2$ . Some of the parameters in the best-fit models change very slightly if different  $[Fe/H]$  and  $[Mg/Fe]$  uncertainties are adopted, but the main conclusions of this paper remain unchanged.

The abundance distribution functions derived from these mock catalogs are then compared to the observed APOGEE catalogs to assess the goodness of match to the data. This assessment is performed with an unweighted quasi- $\chi^2$  diagnostic defined as:

$$\chi_v^2 = \sum_i \frac{(X_{\text{mod},i} - X_{\text{obs},i})^2}{N\bar{\sigma}^2}, \quad (2)$$

where the sum is calculated over all  $[Fe/H]$  and  $[Mg/Fe]$  bins ( $i$ ),  $X_{\text{mod}}$  and  $X_{\text{obs}}$  are the values of the model and observed DFs in each bin, and  $\bar{\sigma}$  is the average Poisson error over all these bins. The quantity  $N$  stands for the degrees of freedom in the fitting, which equals the number of  $[Fe/H]$  and  $[Mg/Fe]$  bins (here, 50) minus the number of free model parameters (5), so for the results described below,  $N = 45$ . We adopt a constant error  $\bar{\sigma}$  in order to use the constraining power of both density peaks and troughs in MDF and  $\alpha$ -DF. The model that minimizes this reduced quasi- $\chi^2$  is considered the best-fit model. Since a constant error is used

**Table 1.** Parameter ranges of the SFH model grid. Quantities in parentheses are the grid step size of each parameter. The first four parameters are described in §3.3 and the fifth in §3.1.

Parameter	Range
$Coe_{\text{burst}}$	0.1-1 (0.1)
$Coe_{\text{post-burst}}$	0.01-0.28 (0.01-0.02)
$t_{\text{acc,tran}}$	0.1-1.5 (0.1)
$t_{\text{SFE,tran}}$	0.6-2.2 (0.2)
$f_{\text{SN-Ia}}$	0.016-0.030 (0.2)

in the  $\chi^2$  calculation, it does not affect the choice of the best-fit model.

### 3.4.2 The best-fit models

Figure 4 shows the  $\chi_v^2$  as a function of each free parameter, with the other four parameters fixed to their best-fit values, for models with K06 yields. Figure 5 shows the equivalent results for the models with CL04 yields. These best-fit parameters and minimized  $\chi_v^2$  values are listed in Table 2.

To illustrate the robustness of the fit, we include  $\chi_v^2$  calculated for the abundance distribution functions on the mid-plane (black dashed line) and for the whole bulge region with and without considering the disk flare (magenta dash-dotted and blue solid lines, respectively). It can be seen that considering the disk flare barely affects the fitting results. This constancy is expected given the very small change in abundance distribution functions when taking the disk flare into consideration (see Fig. 2). It also implies that the fitting results are robust against small variations in the data.

A slightly different model, regardless of CCSNe yield choice, is preferred by the data on the mid-plane. As discussed in §2, compared to the region high above the disk, the mid-plane in the bulge contains relatively more metal-rich, low- $\alpha$  stars and fewer metal-poor, high- $\alpha$  stars. As a result,

models with less star formation in the initial starburst phase (i.e., lower  $Coe_{\text{burst}}$ ) or more star formation in the following prolonged secular phase (i.e., higher  $Coe_{\text{post-burst}}$ ) are favored by the unscaled mid-plane observations. However, the shape of the  $\chi^2_\nu$  distribution of these fits are rather similar, which suggests the model parameters are consistently constrained by the observed abundance distribution functions without strong degeneracy. Note that the sample selected in this work likely underestimates the surface density of the metal-richest stars ( $[\text{Fe}/\text{H}] > +0.2$ ; §2.1), and thus the fraction of the metal-rich, low- $\alpha$  sequence. This implies more star formation in the secular evolution phase than the prediction of the best-fit models presented here. To account for that, a higher post-burst SFE would be required, and some residual gas accretion may also be needed to fuel more star formation. We expect the scale of change in these parameters would be comparable to the difference between the best-fitted models for the observations on the mid-plane and for the whole bulge region which also show considerably different fraction of metal-rich, low- $\alpha$  stars.

Compared to K06 yields, the best-fit model based on CL04 yields has a relatively shorter initial accretion phase and therefore short starburst episode. Another difference is that the SFE is generally higher in the models with CL04 yields. These differences are mainly because  $[\text{Mg}/\text{Fe}]$  in the CL04 yields is  $\sim 0.3$  dex lower than in the K06 yields. With this lower  $[\text{Mg}/\text{Fe}]$  in CCSNe yields, a higher star formation rate is needed to reproduce the observed  $[\text{Mg}/\text{Fe}]$  at a given  $[\text{Fe}/\text{H}]$ . More star formation results in more rapid enrichment and therefore reaching the density gap in  $[\text{Fe}/\text{H}]$  earlier, when the transition of star formation occurs. Although the best-fit values of the parameters are different, the qualitative pictures of the two best-fit star formation scenarios are the same, and the fit quality to the data is comparable. More discussion on this is presented in §4.

Given the consistent model parameters obtained for the original data on the mid-plane and the integrated ones for the whole bulge, hereafter we focus on the two best-fit models, one with K06 yield tables and one with CL04 yields, for the integrated abundance distribution in the bulge that accounts for the disk flare.

### 3.4.3 Evolutionary history of the best-fit models

Figure 6 shows the SFR (upper-left panel), gas accretion (upper-right panel),  $[\text{Fe}/\text{H}]$  (bottom-left panel), and  $[\text{Mg}/\text{Fe}]$  (bottom-right panel) histories of the two best-fit models based on CL04 (orange) and K06 (green) CCSNe yields. The initial gas accretion episode in both models lasts 1 Gyr or less, suggesting the inner Galaxy has evolved largely as a closed-box system. There are two major phases of star formation: a short initial starburst associated with the initial gas accretion, followed by a prolonged secular evolution phase with low-level star formation activity. Similar to the disk model history in Lian et al. (2020a), the early starburst is responsible for generating the metal-poor, high- $\alpha$  branch (i.e., the chemical/geometric inner thick disc), while the metal-rich, low- $\alpha$  branch is slowly built up during the later secular evolution. Therefore, the bulk of the old, metal-poor bulge stars is formed during the short-lived initial starburst. This rapid gas accretion and starburst in the early Universe that forms the bulge is consistent with the picture

of coalescing giant clumps in a turbulent disk that has been proposed as a means of bulge formation in the literature (e.g., Elmegreen et al. 2008; Inoue & Saitoh 2012; Clarke et al. 2019). Other channels can also trigger a short early starburst, including an initial dissipative collapse and/or early hierarchical mergers, which could possibly be involved in the bulge formation.

An important episode shared by both modeled SFHs is the dramatic decrease in SFR right after the peak, which drops by one order of magnitude within 1 Gyr. This rapid SFR cessation (the so-called “quenching”) process is critical to reproduce the observed  $\alpha$ -bimodality (Haywood et al. 2018; Lian et al. 2020a). Interestingly, during this quenching episode, both models favor a two-step decrease of SFR with a relatively slower decline followed by a nearly straight drop. The first step is caused by the shutdown of the external gas supply (transition of gas accretion is earlier than the SFE). The second step, instead, is caused by switching the SFE to a lower values. This two-step cessation of SFR is required to explain the existence of the density bump in the  $\alpha$ -DF. The higher  $[\text{Mg}/\text{Fe}]$  of the metal-poor bulge stars, compared to stars in the thick disk in the solar vicinity, implies that this quenching process likely takes place earlier in the inner Galaxy and then propagates outwards, consistent with the inside-out quenching picture proposed to explain external galaxy observations (Ellison et al. 2018; Wang et al. 2018; Lin et al. 2019).

It is worth pointing out that the well-known bimodality of the general galaxy population in the color–magnitude (or color–mass) diagram—the blue cloud versus the red sequence—is also largely shaped by a rapid SFR cessation process that quiescent galaxies have experienced (e.g., Schawinski et al. 2014; Lian et al. 2016). This similarity to the quenching-induced  $\alpha$ -bimodality in the Milky Way suggests an intriguing link between the evolutionary path of our Galaxy and the general galaxy population, and that the SFR quenching process has been playing a critical role in shaping galaxies observed today, including our Galaxy. We offer a heuristic speculation that, if the recent gas accretion event that supplied metal-poor gas and boosted star formation in the disk (mostly in the outer disc; Lian et al. 2020b) did not happen, our Galaxy would not appear to be star-forming today but instead be quiescent and red, like a S0 galaxy.

## 4 DISCUSSION

### 4.1 A three-phase SFH for the bulge

The SFHs of our best-fit models comprise three phases: an initial starburst, followed by a rapid star formation quenching episode, and a long-term secular evolution phase with a low SFR. Figure 7 shows the integrated  $[\text{Mg}/\text{Fe}]$ – $[\text{Fe}/\text{H}]$  distribution of the whole bulge region and the predicted evolution tracks of our best-fit models. Green solid and orange dashed lines indicate the K06- and CL04-based models, respectively, as in Figure 6. The large black circles highlight important transition times in the models, when the gas accretion switches off and the SFE ramps down. Other circles along the model tracks mark constant time intervals of 0.2 Gyr for the evolution in the first 2 Gyr.

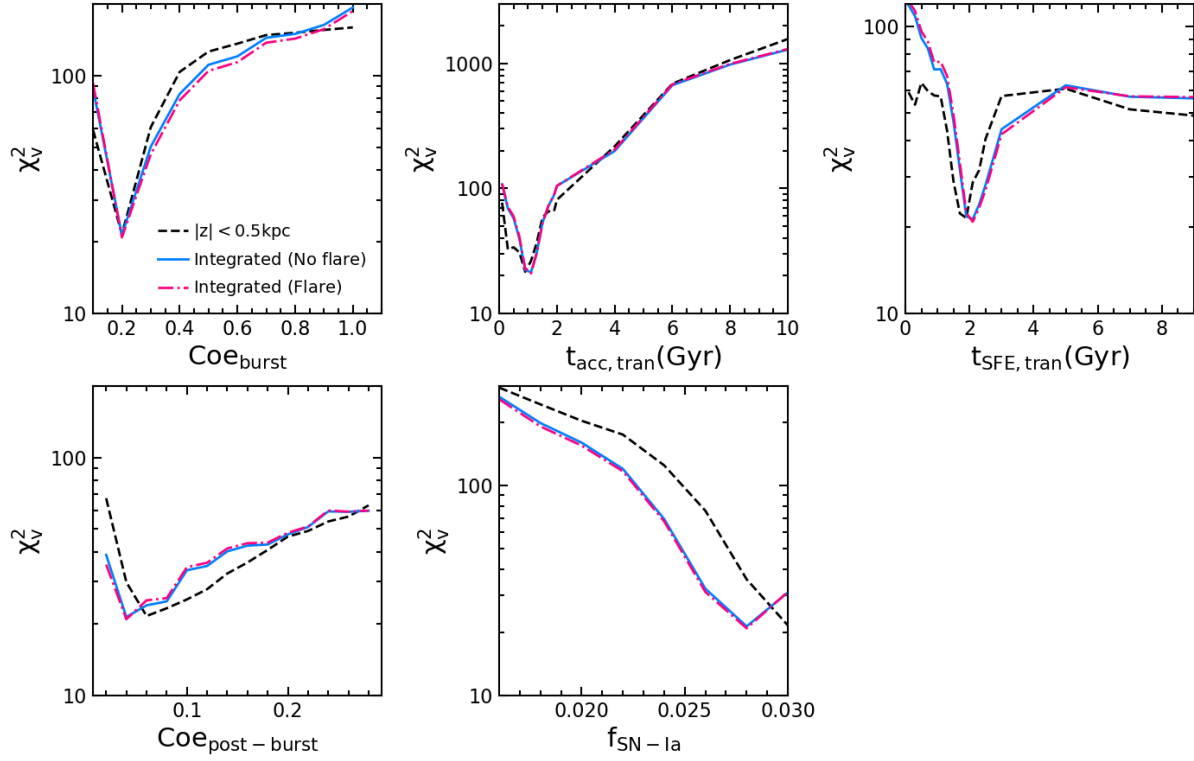


**Figure 4.**  $\chi^2_{\nu}$  distribution as functions of each model parameter, with other parameters fixed to their best-fit values. The CCSNe yields from K06 are used in the models. Fitting results for observations in the mid-plane are shown as black dashed lines, and results for the integrated bulge region, with or without consideration of disk flare, are indicated as with magenta dash-dotted lines and blue solid lines, respectively.

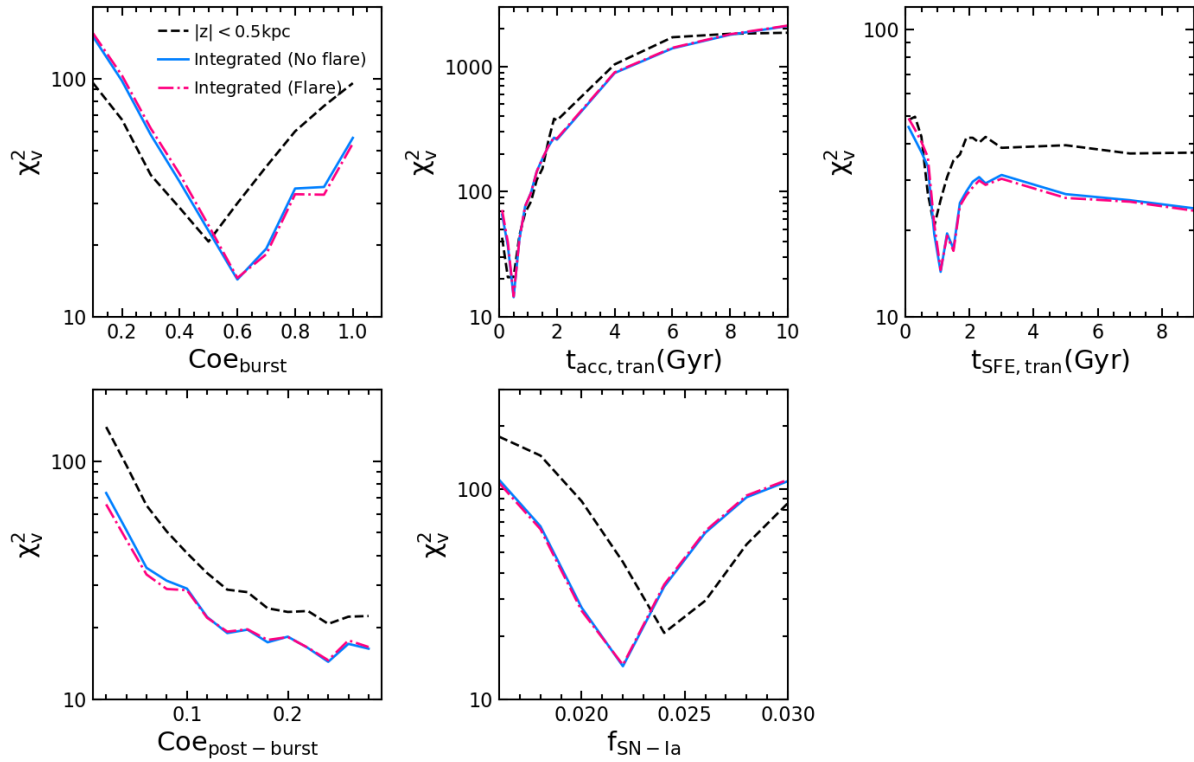


**Figure 5.** Same structure as Fig. 4 but using CL04 CCSNe yields in the model.

**Table 2.** Best-fitting bulge SFH parameters (Table 1) for models based on CCSNe yields from Kobayashi et al. (2006, K06) and Chieffi & Limongi (2004, CL04), fitted to observed abundances distributions on the mid-plane and in the integrated bulge region with and without considering the disk flare. The last column lists the reduced- $\chi^2$  value for each model. The parameters of the “Test model” discussed in §3.2 and shown in Fig.3 are also included.

Model	$Coe_{\text{burst}}$	$Coe_{\text{post-burst}}$	$t_{\text{acc,tran}}$	$t_{\text{SFE,tran}}$	$f_{\text{SN-Ia}}$	$\chi^2_{\nu}$
	-	-	Gyr	Gyr	-	-
K06 (mid-plane)	0.20	0.06	0.9	1.9	0.030	21.5
K06 (no flare)	0.20	0.04	1.1	2.1	0.028	21.3
K06 (flare)	0.20	0.04	1.1	2.1	0.028	20.9
CL04 (mid-plane)	0.50	0.24	0.3	0.9	0.024	20.7
CL04 (no flare)	0.60	0.24	0.5	1.1	0.022	14.3
CL04 (flare)	0.60	0.24	0.5	1.1	0.022	14.6
Test model	1.00	0.2	4.0	4.0	0.028	-

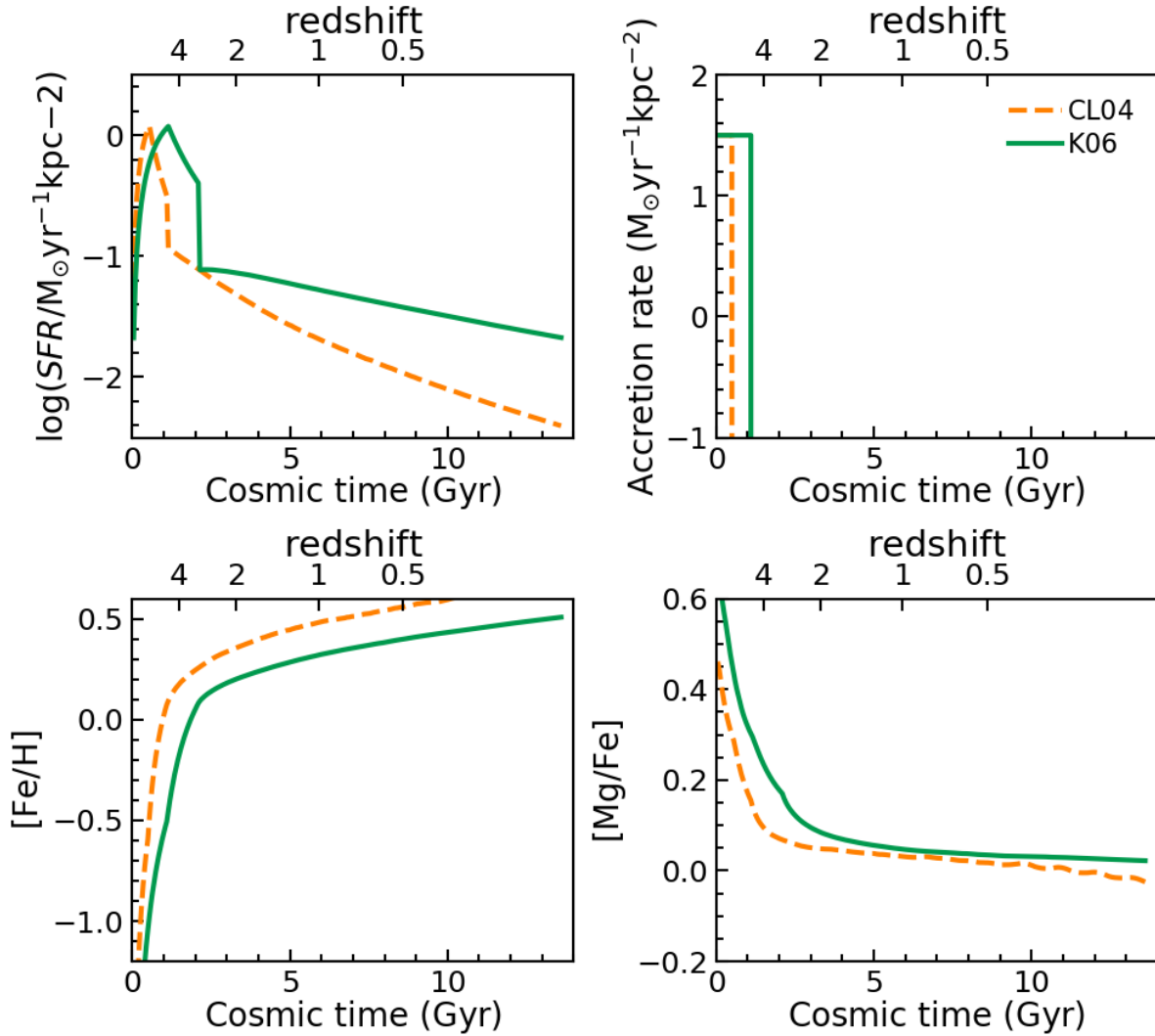


**Figure 6.** SFR (upper-left panel), Gas accretion (upper-right panel),  $[\text{Fe}/\text{H}]$  (bottom-left panel), and  $[\text{Mg}/\text{Fe}]$  (bottom-right panel) histories of best-fit models based on CCSNe yields from K06 (solid green) and CL04 (dashed orange).

Given this three-phase SFH, the  $[\text{Mg}/\text{Fe}]$ – $[\text{Fe}/\text{H}]$  diagram can be separated into three general regimes (vertical dashed lines in Figure 7). The metal-poor, high- $\alpha$  branch is mostly formed during the initial starburst. The following density valley between the high- and low- $\alpha$  branches is due to a rapid star formation quenching process. The metal-rich, low- $\alpha$  branch is gradually built through low SFR in the long-term secular evolution phase. This interpretation suggests that the density gap between the two main branches represents a transition between two modes of star formation in the bulge, from violent, bursty star formation at early times to long-term, low-state star formation more recently. This transition is qualitatively similar to the transition of disk formation from the chemical thick to the chemical thin disk (Haywood et al. 2018; Lian et al. 2020a) except for an earlier onset in the inner Galaxy.

#### 4.2 Comparison with earlier bulge SFH measurements

To account for the complex MDF in the bulge, a multi-phase SFH framework is generally adopted in the literature (Tsujiimoto & Bekki 2012; Grieco et al. 2012; Haywood et al. 2018; Matteucci et al. 2019). The metal-poor bulge stars are generally believed to build up quickly at early times, while the metal-rich stars formed with a relatively longer time scale (Tsujiimoto & Bekki 2012; Grieco et al. 2012). Haywood et al. (2018) argued that a multi-phase SFH involving a rapid quenching stage adopted from Snaith et al. (2015) could both explain well the global  $[\text{Mg}/\text{Fe}]$ – $[\text{Fe}/\text{H}]$  relation and broadly reproduce the  $\alpha$ -bimodality in the inner Galaxy. By comparing the model-predicted MDF and  $\alpha$ -DF with observations, they concluded that the star formation quenching process is critical to reproduce the density dip between the high- and low- $\alpha$  branches. This empirical result is qualitatively consistent with our quantitative result.

However, the SFH proposed in Haywood et al. (2018) is quantitatively different from the SFH in our best-fit model. The early starburst of Haywood et al. (2018) lasts  $\sim 1$  Gyr longer, and the quenching episode starts much later, than in our bulge SFH ( $\sim 4$  Gyr versus  $\sim 1$  Gyr after initial star formation). The model in Haywood et al. (2018) also faces challenges reproducing the observed MDF and  $\alpha$ -DF in detail, such as the relative number of high- and low- $\alpha$  stars.

An alternative scenario to explain the MDF in the bulge is a bursty SFH, as proposed by Matteucci et al. (2019). In this scenario, the bulge SFH consists of multiple, short-lived starbursts that are separated by non-star forming gaps. This SFH is shown to be able to reproduce multiple peaks in the bulge MDF (Bensby et al. 2017). A strong prediction of this scenario is a complex  $\alpha$ -DF, possibly with numerous peaks, that is inconsistent with the clear double-peaked bulge  $\alpha$ -DF as shown in this and other works.

In addition to chemical evolution modelling, a large number of bulge SFHs have been derived using different methodologies (Nataf 2016). Most previous work relying on chemical compositions or photometric age estimates suggest that the bulge is a generally old component (Zoccali et al. 2003; Grieco et al. 2012). However, the inferred age distribution of bulge planetary nebulae peaks around  $\sim 3$  Gyr, suggesting the presence of a considerable fraction of young

populations in the bulge (Buell 2013; Gesicki et al. 2014), a finding consistent with other photometric and spectroscopic studies (e.g., Bensby et al. 2013; Bernard et al. 2018), and also present in barred galaxies in cosmological simulations of (Fragkoudi et al. 2020). A recent study of spectroscopic ages of bulge stars (Hasselquist et al., in prep) also confirms a non-negligible fraction of young stars (age  $\sim 2$ – $5$  Gyr) that are preferentially found in the plane.

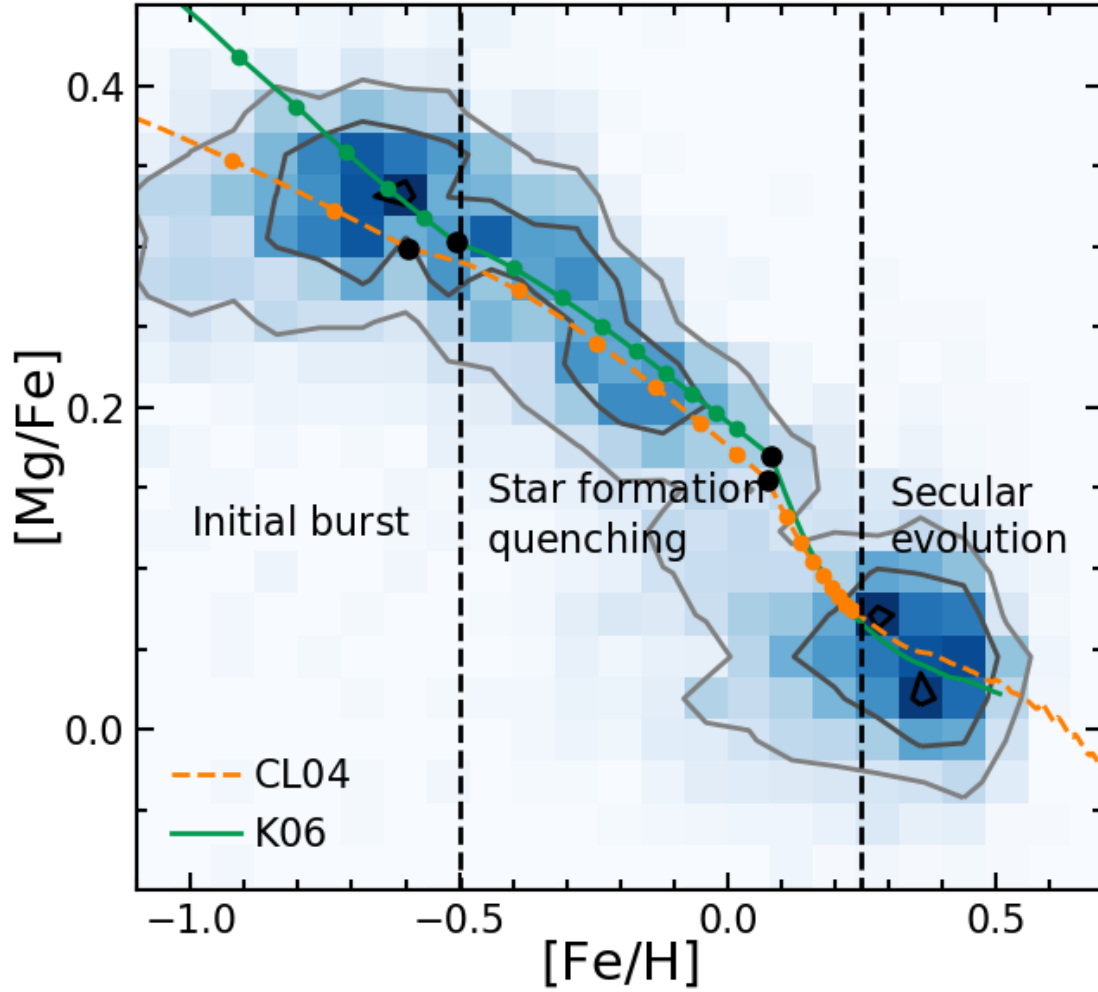
The bulk bulge population predicted by our best-fit SFH is generally old, with a mass-weighted integrated stellar age of 10.5 and 9.7 Gyr for models with CL04 and K06 yields, respectively. However, we note that a significant fraction of young stars is also predicted. Figure 8 shows the predicted age distribution of our best-fit models assuming an age uncertainty of 0.25 dex. The left-hand panel indicates the global age distribution while the right-hand sub-panels show age distribution in four metallicity bins that correspond to the metallicity range of each episode in the best-fit SFH. The two intermediate metallicity bins correspond to the two stages of the star formation quenching phase. The ages are derived based on a simple assumption that the star formation in the protogalaxy that would become the Milky Way started at 13.7 Gyr ago.

Given an age uncertainty of 0.25 dex, the number fraction of living young stars (age  $< 5$  Gyr) predicted by the best-fit models are 11.3% and 15.8% for CL04 and K06 CC-SNe yields, respectively. Note that this fraction is subject to change when different age uncertainty is assumed. For example, a considerably higher fraction of 25–29% is expected when assuming an age uncertainty of 0.4 dex. Comparing to the age distribution predicted by four distinct bulge SFHs as shown in Fig. 1 in Nataf (2016), our result is more consistent with the age distribution derived by Bensby et al. (2013).

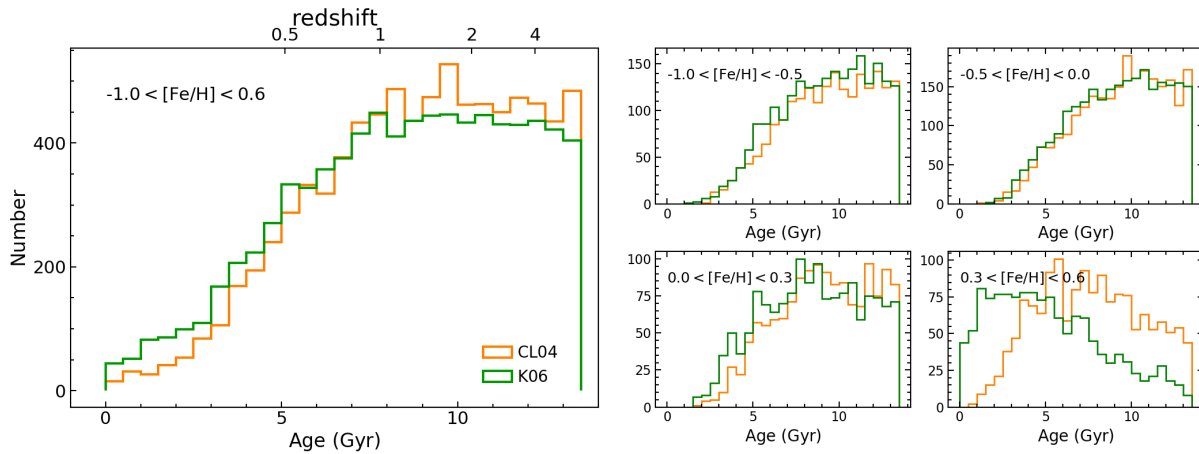
#### 4.3 Room for improvement in the model

Figure 9 shows the density distribution of  $[\text{Mg}/\text{Fe}]$ – $[\text{Fe}/\text{H}]$  as predicted by our best-fit models. The observed stellar distribution is shown as orange contours for comparison. Both models reproduce the global  $[\text{Mg}/\text{Fe}]$ – $[\text{Fe}/\text{H}]$  trend and the  $\alpha$ -bimodality remarkably well. A noticeable difference is the narrowness of the tracks predicted by the models, compared to the data, in both low- and high- $\alpha$  branches. Figure 10 compares the observed and predicted MDF and  $\alpha$ -DF for the best-fit models. The matches to the observed abundance distribution functions are equally good for these two models. The bimodal  $\alpha$ -DF is reproduced remarkably well, including the bump at  $[\text{Mg}/\text{Fe}] \sim 0.2$ . The bimodality in  $[\text{Fe}/\text{H}]$  predicted by the models is also less significant than that in  $[\text{Mg}/\text{Fe}]$ , with an extended tail at the metal-poor end, which is in good consistency with observations.

Nevertheless, there remains room for improvement in the model fits to the abundance distribution functions. The low metallicity peaks in the MDF predicted by the models are slightly offset towards higher metallicity ( $\sim -0.6$  versus observational  $\sim -0.7$ ). This is a result of trade-offs to match the  $[\text{Mg}/\text{Fe}]$  distribution at the same time. Another under-performance in the models is that the predicted width of the low- $\alpha$  population in the  $[\text{Mg}/\text{Fe}]$  distribution is narrower than the data. This is also visible in Fig. 9. One possible reason for this discrepancy could be that the obser-



**Figure 7.** Integrated  $[\text{Mg}/\text{Fe}]$ – $[\text{Fe}/\text{H}]$  distribution of the bulge region, overlplotted with the evolution tracks of best-fit models based on K06 (green solid) and CL04 (orange dashed) yields (§3.4). Orange and green circles on the model tracks mark time intervals of 0.2 Gyr for evolution in the first 2 Gyr. Larger black circles highlight the important transitions of gas accretion and SFE in the model. Vertical dashed lines separate the three primary phases of star formation, as discussed in the text.



**Figure 8.** Global age distribution (left-hand panel) and that in four metallicity bins (right-hand panels) predicted by the best-fit models based on CL04 and K06 CCSNe yields. A notable fraction of young stars (age < 5 Gyr), which are preferentially very metal-rich, is present.

vational uncertainties adopted in the model simulations are still underestimated. Another possibility is that the residual scatter is intrinsic, which suggests that the evolution path may not be smooth and unique but rather (at least somewhat) stochastic and inhomogeneous. The SFH implied by the best-fit models in this work could be considered as an average solution. To account for stochasticity in SFH requires a much more complex star formation framework, which is beyond the scope of this paper aiming at understanding the global bulge SFH.

Although our sample does not cover the low metallicity range ( $[\text{Fe}/\text{H}] < -1.2$ ), our best-fit models, especially the one with the K06 yields, keep increasing with decreasing  $[\text{Fe}/\text{H}]$  at  $[\text{Fe}/\text{H}] < -1$ . This is not consistent with the observed flat  $[\text{Mg}/\text{Fe}]$  plateau at  $[\text{Fe}/\text{H}] < -1$  in many other previous works (e.g. McWilliam et al. 1995). The models also seem to not reproduce well the “knee” (change of slope) at  $[\text{Fe}/\text{H}] \sim -0.6$ . We hypothesize this mismatch is possibly due to the original  $[\text{Mg}/\text{Fe}]$  ratio in the CCSNe yields at low metallicity not matching the  $[\text{Mg}/\text{Fe}]$  value of the plateau, and/or the adopted minimum SN-Ia delay time being too low.

To test this latter idea, we calculated another set of test models, named ‘late-Ia’ models here, for each of the CCSNe yields, adopting a higher minimum SN-Ia delay time (150 Myr for CL04 and 70 Myr for the K06 yields), the default yield tables (i.e., no Mg enhancement), and lower fractions of SN-Ia progenitors (0.012 for CL04 and 0.018 for K06 yields), which are required for the default Mg production to match the  $[\text{Mg}/\text{Fe}]$  of the low- $\alpha$  sequence. The value of minimum SN-Ia delay time is adopted for an example to demonstrate the impact of changing SN-Ia DTD, and all the other changes have to happen at the same time to maintain the  $[\text{Mg}/\text{Fe}]$ - $[\text{Fe}/\text{H}]$  trend. The SFH of these late-Ia models are adopted as the same as the corresponding best-fit models. Figure 11 shows the evolutionary track of the late-Ia models in the  $[\text{Mg}/\text{Fe}]$ - $[\text{Fe}/\text{H}]$  plane. The predicted MDF and  $\alpha$ -DF, compared with the observed data, are shown in Figure 12. It can be seen that these late-Ia models reproduce well the global  $[\text{Mg}/\text{Fe}]$ - $[\text{Fe}/\text{H}]$  trend, and indeed show a more pronounced “knee” at  $[\text{Fe}/\text{H}] \sim -0.6$  and tend to flatten at lower metallicity.

However, the predicted abundance distribution functions do not match the observed ones as well as the best-fit models with a lower minimum SN-Ia delay time. The predicted MDF shifts systematically towards lower  $[\text{Fe}/\text{H}]$ . We have tested that the under-performance of late-Ia models remains when allowing SFH to vary. Since we focus on APOGEE observations in this work, we present the best-fit models to those data as our fiducial models. However, these late-Ia models illustrate one direction of future improvements when more observations of metal-poor stars are used to constrain the chemical evolution history.

## 5 SUMMARY

We investigate the star formation history of the Galactic bulge by quantitatively modelling the  $[\text{Fe}/\text{H}]$  and  $[\text{Mg}/\text{Fe}]$  distribution functions simultaneously and matching to observations from the APOGEE survey. To avoid potential bias introduced by the varying sampling of the APOGEE survey

at different vertical distances, we select our sample close to the mid-plane ( $|z| < 0.5$  kpc) and account for the vertical structure of mono-abundance sub-populations as in Bovy et al. (2012, 2016) to infer integrated abundance distribution functions. A major effect of accounting for the vertical structure is an increase in the number of metal-poor, high- $\alpha$  stars with respect to the metal-rich, low- $\alpha$  stars because of the former’s larger scale height.

In both the raw and integrated  $[\text{Mg}/\text{Fe}]$  distribution functions, a clear bimodal distribution is present, with peaks at +0.03 and +0.33 dex and a gap at +0.15 dex. An interesting weak bump is also present at +0.2 dex. The integrated  $[\text{Fe}/\text{H}]$  distribution function exhibits three peaks at  $\sim -0.67$ ,  $\sim -0.27$  and  $\sim +0.37$  dex with a dip at solar metallicity.

To extract SFH information from abundance distribution functions, we apply our numerical chemical evolution model based on a star formation framework that allows single or multiple phases of star formation. To fully exploit the data, we explore a wide parameter space and systematically search for the best-fit model based on a quantitative assessment of fit quality. We obtain the best-fit model for the observations on the mid-plane as well as for the integrated ones across the global bulge region. To test the effect of stellar yields on the results, we run two sets of models with different CCSNe yields (from K06 and CL04) and describe both sets of best-fit results.

The best-fit models, regardless of the CCSNe yields used, suggest a three-phase SFH that consists of an early and intense starburst, followed by a rapid star formation quenching episode (one order of magnitude decrease in SFR within 1 Gyr), and a prolonged stage of low star formation. The early starburst is responsible for the formation of the metal-poor, high- $\alpha$  branch; during the prolonged third phase, the metal-rich, low- $\alpha$  branch is gradually built up. These two star formation phases are connected by a rapid star formation quenching episode (an order of magnitude decrease in SFR within  $\sim 1$  Gyr) that occurs in the early Universe. Because of the rapid decrease in SFR, the  $[\text{Mg}/\text{Fe}]$  ratio in the ISM also drops significantly and rapidly, leaving few stars formed with intermediate  $[\text{Mg}/\text{Fe}]$ . This quenching process is therefore critical to reproduce the  $\alpha$ -bimodality observed in the Milky Way, not only in the bulge region but also in the disk (Lian et al. 2020a). Future work will further address whether this quenching process took place simultaneously throughout the Galaxy or propagated inside-out or outside-in by studying radial variation of abundance distribution functions in more detail. Given the best-fit SFH in this work, a non-negligible fraction of young stars (age  $< 5$  Gyr) is expected to exist in the bulge, a prediction that is broadly consistent with several recent age determinations of bulge stars (e.g., Bernard et al. 2018, Hasselquist et al., in prep).

There are mild differences between the best-fit models when using K06’s or CL04’s CCSNe yields. In general, the model with CL04 yields requires a higher SFE in both star formation phases to balance the lower intrinsic  $[\text{Mg}/\text{Fe}]$  in the yields table. However, the main characteristics of the three-phase SFH are not affected by the choice of CCSNe yields. We conclude that the uncertainty in CCSNe yields mildly affects the best-fit parameter values but does not significantly weaken the constraining power of observed abundance distributions on the bulge’s SFH.

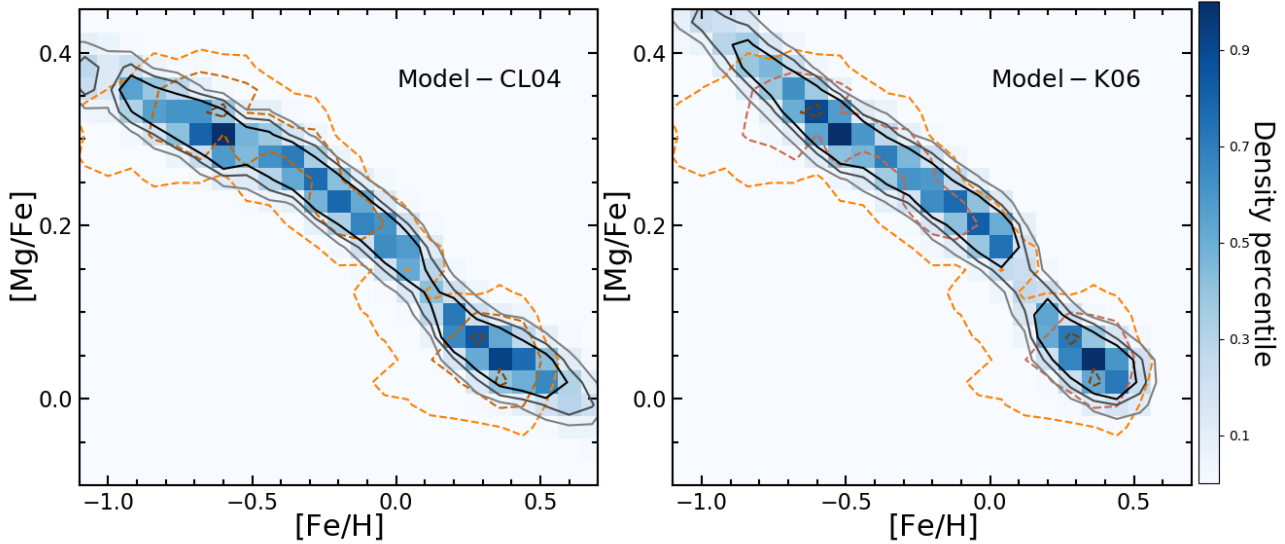


**Figure 9.** Density distribution of  $[\text{Mg}/\text{Fe}]$ – $[\text{Fe}/\text{H}]$  as predicted by the best-fit models for CL04 yields (left-hand panel) and K06 yields (right-hand panel). The observed distribution for the whole bulge region is overplotted as orange dashed contours for comparison.

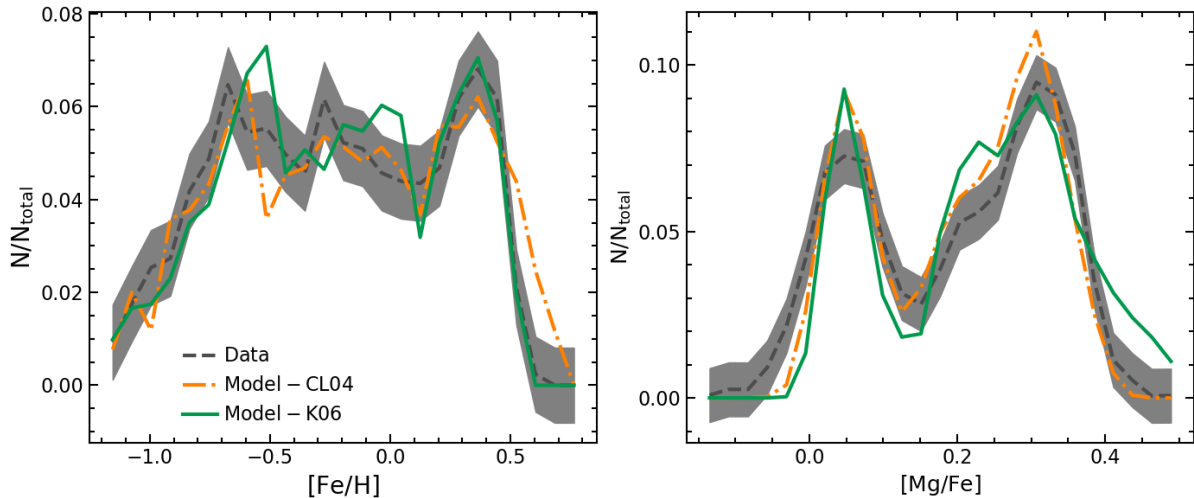


**Figure 10.** Comparison between the observed and modeled  $[\text{Fe}/\text{H}]$  (left-hand panel) and  $[\text{Mg}/\text{Fe}]$  (right-hand panel) distribution functions. The gray shaded region indicates the  $3\sigma$  scatter of the observed MDF and  $\alpha$ -DF, representing the average Poisson uncertainty used to calculate the  $\chi^2$  in Eq. 2.

## ACKNOWLEDGEMENTS

ARL acknowledge partial financial support to the APOGEE2-S survey through the QUIMAL project 130001 and FONDECYT project 1170476. DMN acknowledges support from NASA under award Number 80NSSC19K0589.

Funding for the Sloan Digital Sky Survey IV has been provided by the Alfred P. Sloan Foundation, the U.S. Department of Energy Office of Science, and the Participating Institutions. SDSS-IV acknowledges support and resources from the Center for High-Performance Computing at the University of Utah. The SDSS web site is [www.sdss.org](http://www.sdss.org).

SDSS-IV is managed by the Astrophysical Research Consortium for the Participating Institutions of the SDSS Collaboration including the Brazilian Participation Group,

the Carnegie Institution for Science, Carnegie Mellon University, the Chilean Participation Group, the French Participation Group, Harvard-Smithsonian Center for Astrophysics, Instituto de Astrofísica de Canarias, The Johns Hopkins University, Kavli Institute for the Physics and Mathematics of the Universe (IPMU) / University of Tokyo, the Korean Participation Group, Lawrence Berkeley National Laboratory, Leibniz Institut für Astrophysik Potsdam (AIP), Max-Planck-Institut für Astronomie (MPIA Heidelberg), Max-Planck-Institut für Astrophysik (MPA Garching), Max-Planck-Institut für Extraterrestrische Physik (MPE), National Astronomical Observatories of China, New Mexico State University, New York University, University of Notre Dame, Observatório Nacional / MCTI, The Ohio

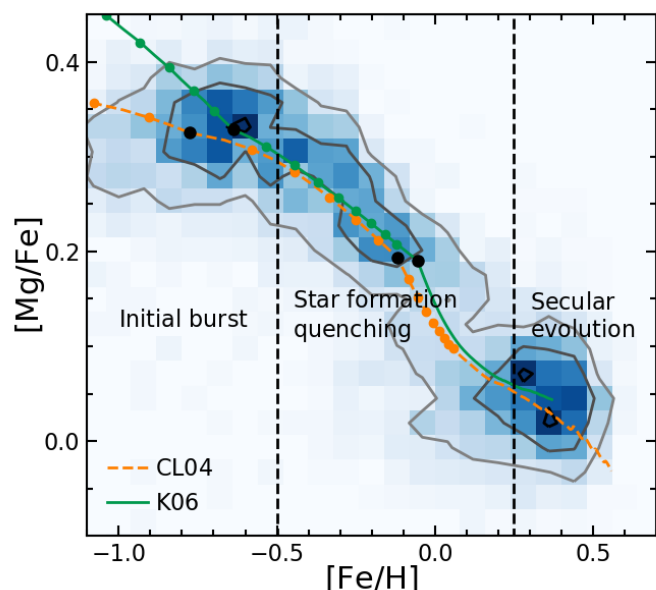


**Figure 11.** The same as Fig.7 except that a higher minimum SN-Ia delay time and default Mg production are assumed for the models.

State University, Pennsylvania State University, Shanghai Astronomical Observatory, United Kingdom Participation Group, Universidad Nacional Autónoma de México, University of Arizona, University of Colorado Boulder, University of Oxford, University of Portsmouth, University of Utah, University of Virginia, University of Washington, University of Wisconsin, Vanderbilt University, and Yale University.

#### DATA AVAILABILITY STATEMENTS

The data underlying this article is from an internal incremental release of SDSS-IV/APOGEE survey, following the SDSS-IV Data Release 16. This incremental release is not publicly available now but will be included in the final public data release of SDSS-IV in 2021. The chemical evolution model results are available upon request.

#### REFERENCES

- Ahumada R., et al., 2020, *ApJS*, 249, 3  
 Alves-Brito A., Meléndez J., Asplund M., Ramírez I., Yong D., 2010, *A&A*, 513, A35  
 Babusiaux C., et al., 2010, *A&A*, 519, A77  
 Bekki K., Tsujimoto T., 2011, *MNRAS*, 416, L60  
 Bensby T., et al., 2013, *A&A*, 549, A147  
 Bensby T., et al., 2017, *A&A*, 605, A89  
 Bernard E. J., Schultheis M., Di Matteo P., Hill V., Haywood M., Calamida A., 2018, *MNRAS*, 477, 3507  
 Blanton M. R., et al., 2017, *AJ*, 154, 28  
 Bovy J., Rix H.-W., Liu C., Hogg D. W., Beers T. C., Lee Y. S., 2012, *ApJ*, 753, 148  
 Bovy J., Rix H.-W., Schlafly E. F., Nidever D. L., Holtzman J. A., Shetrone M., Beers T. C., 2016, *ApJ*, 823, 30  
 Bowen I. S., Vaughan A. H. J., 1973, *ApOpt*, 12, 1430  
 Buell J. F., 2013, *MNRAS*, 428, 2577  
 Chieffi A., Limongi M., 2004, *ApJ*, 608, 405  
 Chisholm J., Tremonti C., Leitherer C., 2018, *MNRAS*, 481, 1690  
 Clarke A. J., et al., 2019, *MNRAS*, 484, 3476  
 Cunha K., Smith V. V., 2006, *ApJ*, 651, 491  
 Di Matteo P., Haywood M., Lehnert M. D., Katz D., Khoperskov S., Snaith O. N., Gómez A., Robichon N., 2019, *A&A*, 632, A4  
 Ellison S. L., Sánchez S. F., Ibarra-Medel H., Antonio B., Mendel J. T., Barrera-Ballesteros J., 2018, *MNRAS*, 474, 2039  
 Elmegreen B. G., Bournaud F., Elmegreen D. M., 2008, *ApJ*, 688, 67  
 Fragkoudi F., Di Matteo P., Haywood M., Schultheis M., Khoperskov S., Gómez A., Combes F., 2018, *A&A*, 616, A180  
 Fragkoudi F., et al., 2020, *MNRAS*, 494, 5936  
 Fulbright J. P., McWilliam A., Rich R. M., 2007, *ApJ*, 661, 1152  
 García Pérez A. E., et al., 2016, *AJ*, 151, 144  
 García Pérez A. E., et al., 2018a, *ApJ*, 852, 91  
 García Pérez A. E., et al., 2018b, *ApJ*, 852, 91  
 Gesicki K., Zijlstra A. A., Hajduk M., Szyszka C., 2014, *A&A*, 566, A48  
 Grieco V., Matteucci F., Pipino A., Cescutti G., 2012, *A&A*, 548, A60  
 Gunn J. E., et al., 2006, *AJ*, 131, 2332  
 Hayden M. R., et al., 2015, *ApJ*, 808, 132  
 Haywood M., Di Matteo P., Lehnert M., Snaith O., Fragkoudi F., Khoperskov S., 2018, *A&A*, 618, A78  
 Hill V., et al., 2011, *A&A*, 534, A80  
 Inoue S., Saitoh T. R., 2012, *MNRAS*, 422, 1902  
 Iwamoto K., Brachwitz F., Nomoto K., Kishimoto N., Umeda H., Hix W. R., Thielemann F.-K., 1999, *ApJS*, 125, 439  
 Johnson C. I., McWilliam A., Rich R. M., 2013, *ApJL*, 775, L27  
 Jönsson H., et al., 2018, *AJ*, 156, 126  
 Jönsson H., et al., 2020, arXiv e-prints, p. arXiv:2007.05537  
 Kennicutt Robert C. J., 1998, *ApJ*, 498, 541  
 Kobayashi C., Umeda H., Nomoto K., Tominaga N., Ohkubo T., 2006, *ApJ*, 653, 1145  
 Kroupa P., 2001, *MNRAS*, 322, 231  
 Lecureur A., Hill V., Zoccali M., Barbuy B., Gómez A., Minniti D., Ortolani S., Renzini A., 2007, *A&A*, 465, 799  
 Lian J., Yan R., Zhang K., Kong X., 2016, *ApJ*, 832, 29  
 Lian J., Thomas D., Maraston C., Goddard D., Comparat J., Gonzalez-Perez V., Ventura P., 2018a, *MNRAS*, 474, 1143  
 Lian J., et al., 2018b, *MNRAS*, 476, 3883  
 Lian J., Thomas D., Maraston C., 2018c, *MNRAS*, 481, 4000  
 Lian J., Thomas D., Li C., Zheng Z., Maraston C., Bizyaev D., Lane R. R., Yan R., 2019, *MNRAS*, 489, 1436  
 Lian J., et al., 2020a, arXiv e-prints, p. arXiv:2007.03687  
 Lian J., et al., 2020b, *MNRAS*, 494, 2561  
 Limongi M., Chieffi A., 2018, *ApJS*, 237, 13  
 Lin L., et al., 2019, *ApJ*, 872, 50  
 Mackereth J. T., et al., 2017, *MNRAS*, 471, 3057  
 Majewski S. R., et al., 2017, *AJ*, 154, 94  
 Maoz D., Mannucci F., Brandt T. D., 2012, *MNRAS*, 426, 3282

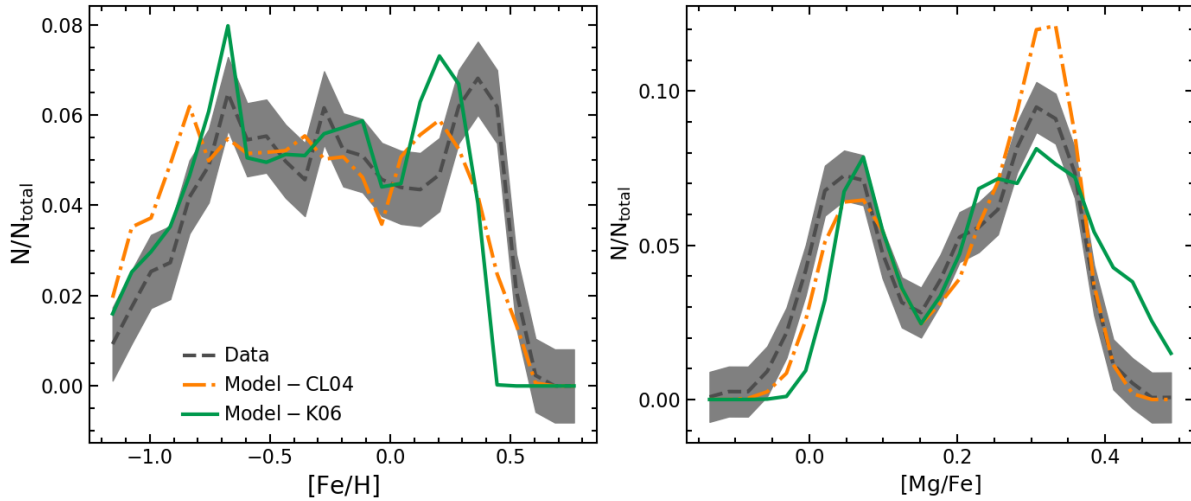


**Figure 12.** The same as Fig.10 except that a higher minimum SN-Ia delay time and default Mg production are assumed for the models.

- Matteucci F., 1994, *A&A*, 288, 57
- Matteucci F., Brocato E., 1990, *ApJ*, 365, 539
- Matteucci F., Spitoni E., Recchi S., Valiante R., 2009, *A&A*, 501, 531
- Matteucci F., Grisoni V., Spitoni E., Zulianello A., Rojas-Arriagada A., Schultheis M., Ryde N., 2019, *MNRAS*, 487, 5363
- Matteucci F., Vasini A., Grisoni V., Schultheis M., 2020, arXiv e-prints, p. arXiv:2004.10133
- McWilliam A., Rich R. M., 1994, *ApJS*, 91, 749
- McWilliam A., Preston G. W., Sneden C., Searle L., 1995, *AJ*, 109, 2757
- Meléndez J., et al., 2008, *A&A*, 484, L21
- Nataf D. M., 2016, *PASA*, 33, e023
- Nataf D. M., 2017, *PASA*, 34, e041
- Ness M., et al., 2013, *MNRAS*, 430, 836
- Nidever D. L., et al., 2014, *ApJ*, 796, 38
- Nidever D. L., et al., 2015, *AJ*, 150, 173
- Portail M., Wegg C., Gerhard O., Ness M., 2017, *MNRAS*, 470, 1233
- Queiroz A. B. A., et al., 2020, *A&A*, 638, A76
- Rich R. M., 1988, *AJ*, 95, 828
- Rich R. M., Origlia L., Valenti E., 2012, *ApJ*, 746, 59
- Rojas-Arriagada A., et al., 2014, *A&A*, 569, A103
- Rojas-Arriagada A., et al., 2017, *A&A*, 601, A140
- Rojas-Arriagada A., Zoccali M., Schultheis M., Recio-Blanco A., Zasowski G., Minniti D., Jönsson H., Cohen R. E., 2019, *A&A*, 626, A16
- Rybizki J., Just A., Rix H.-W., 2017, *A&A*, 605, A59
- Schawinski K., et al., 2014, *MNRAS*, 440, 889
- Schultheis M., et al., 2017, *A&A*, 600, A14
- Snaith O., Haywood M., Di Matteo P., Lehnert M. D., Combes F., Katz D., Gómez A., 2015, *A&A*, 578, A87
- Sukhbold T., Ertl T., Woosley S. E., Brown J. M., Janka H. T., 2016, *ApJ*, 821, 38
- Thomas D., Greggio L., Bender R., 1998, *MNRAS*, 296, 119
- Thomas D., Maraston C., Schawinski K., Sarzi M., Silk J., 2010, *MNRAS*, 404, 1775
- Tsujimoto T., Bekki K., 2012, *ApJ*, 747, 125
- Uttenthaler S., Schultheis M., Nataf D. M., Robin A. C., Lebzelter T., Chen B., 2012, *A&A*, 546, A57
- Ventura P., Di Criscienzo M., Carini R., D’Antona F., 2013, *MNRAS*, 431, 3642
- Wang E., et al., 2018, *ApJ*, 856, 137
- Wegg C., Gerhard O., 2013, *MNRAS*, 435, 1874
- Whitford A. E., Rich R. M., 1983, *ApJ*, 274, 723
- Wilson J. C., et al., 2019, *PASP*, 131, 055001
- Zasowski G., et al., 2013, *AJ*, 146, 81
- Zasowski G., et al., 2017, *AJ*, 154, 198
- Zasowski G., et al., 2019, *ApJ*, 870, 138
- Zoccali M., et al., 2003, *A&A*, 399, 931
- Zoccali M., et al., 2006, *A&A*, 457, L1
- Zoccali M., Hill V., Lecureur A., Barbuy B., Renzini A., Minniti D., Gómez A., Ortolani S., 2008, *A&A*, 486, 177
- Zoccali M., et al., 2017, *A&A*, 599, A12

This paper has been typeset from a  $\text{\TeX}$ / $\text{\LaTeX}$  file prepared by the author.